aerospace

MDPI

Article

Coupled Fluid-Thermal Investigation on Drag and Heat Reduction of a Hypersonic Spiked Blunt Body with an Aerodisk

Bing Fan and Jie Huang *

College of Aerospace Engineering, Nanjing University of Aeronautics and Astronautics, Nanjing 210016, China; pangningyu@163.com
* Correspondence: jiehuangxyz@163.com

Abstract: In the traditional investigations on the drag and heat reduction of hypersonic spiked models, only the aerodynamic calculation is performed, and the structural temperature cannot be obtained. This paper adopted the loosely coupled method to study its efficiency of drag and heat reduction, in which the feedback effect of wall temperature rise on aeroheating is considered. The aeroheating and structural temperature were obtained by the CFD and ABAQUS software respectively. The coupling analysis of the hypersonic circular tube was carried out to verify the accuracy of the fluid field, the structural temperature, and the coupled method. Compared with experimental results, the calculated results showed that the relative errors of stagnation heat flux and stagnation temperature were 1.34% and 4.95% respectively, and thus the effectiveness of the coupled method was verified. Installing a spike reduced the total drag of the forebody. The spiked model with an aerodisk reduced the aeroheating of the forebody, while the model without an aerodisk intensified the aeroheating. The spiked model with a planar aerodisk had the best performance on drag and heat reduction among all the models. In addition, increasing the length of the spike reduced the drag and temperature of the forebody. With the increase of the length, the change rates of drag, pressure, heat flux, and temperature decreased gradually. Increasing the diameter of the aerodisk also reduced the temperature of the forebody, while the efficiency of forebody drag reduction first increased and then decreased. In conclusion, the heat and drag reduction must be considered comprehensively for the optimal design of the spike.

Keywords: coupled method; spike; aeroheating; drag; hypersonic

Citation: Fan, B.; Huang, J. Coupled Fluid-Thermal Investigation on Drag and Heat Reduction of a Hypersonic Spiked Blunt Body with an Aerodisk. *Aerospace* **2022**, *9*, 19. https://doi.org/10.3390/aerospace9010019

Academic Editor: Sergey Leonov

Received: 12 November 2021
Accepted: 22 December 2021
Published: 30 December 2021

1. Introduction

The aeroheating and wave drag are the most important features of hypersonic vehicles [1,2]. The measurements of the drag reduction and thermal protection must be taken into consideration to ensure a better flight condition and also to ensure the safety of hypersonic vehicles. The traditional thermal protection system (TPS) is mainly passive, such as the ceramic TPS and metal TPS [3–5]. Although the passive TPS has been widely used in hypersonic vehicles, it can not reduce aerodynamic drag. The active TPS based on flow control can simultaneously reduce aeroheating and aerodynamic drag, which has been a research hot spot in recent years.

The spike is a type of active TPS based on the flow control. The mechanism destroys the bow shock wave generated by the forebody and changes it into oblique shock [6–8]. The free stream is firstly compressed by the spike, and then its speed decreases. The air flows downstream and is subjected to secondary compression by the forebody, thus forming a reattached shock wave. The reattached point is the thermal danger point of the forebody [9,10]. The flow characteristics and mechanisms of the aerodisk/spike model were studied by the numerical and experimental methods [11–13]. The aerodisk is usually installed at the front of the spike; it enhances the compression to free stream and reduces the aeroheating and aerodynamic drag more effectively. However, the spike has some

disadvantages. The stagnation heat flux of the spike is high enough to burn the spike in hypersonic flow, rendering the spike not reusable [14–16]. In addition, the spike changes the aerodynamic shapes of original vehicles.

The opposing jet is another type of active TPS based on the flow control, and the nozzle of the forebody can eject high-pressure gas [17–19]. On the one hand, the opposing jet can weaken shock wave, and this function is similar to the spike. On the other hand, the ejected gas is usually cold enough to cool the forebody actively. Therefore, the opposing jet reduces the temperature of the forebody through the combined action of the above two ways [20–22]. Some scholars have validated the efficiency of the opposing jet by numerical and experimental methods. Huang et al. [23] used the numerical method to study the influence of the penetration mode on thermal protection efficiency. Hayashi et al. [20] used the experimental method to measure the heat flux of forebody with the opposing jet, and the jet gas adopted was nitrogen.

For further reducing the aeroheating and aerodynamic drag, some scholars have designed some combined configurations by taking advantage of both the opposing jet and the spike [24–29]. On this basis, the combined configuration of the spike and the lateral jet is developed [30]. The numerical and experimental investigations show that the combined configurations have reached a higher efficiency of drag and heat reduction.

The previous scholars mainly studied the mechanism and performance of the above configurations through experimental and numerical methods from the perspective of flow field, while the structural temperature is one the most important factors to consider in the design of thermal protection, which directly affects the safety of the vehicles. This paper studied the thermal protection efficiency of the spiked model by adopting the fluid-thermal coupled method, which can calculate the wall heat flux and structural temperature directly.

2. Coupled Fluid-Thermal Numerical Method

2.1. Coupling Strategy

The aeroheating causes the structural temperature to rise sharply, and the high temperature will result in the decrease of aeroheating according to the Fourier's law. This paper adopted the loosely coupled method to analyze the structural thermal environment (Figure 1). The aeroheating and structural temperature were obtained by the CFD and ABAQUS software respectively. In addition, the fluid and structural grids are usually different in size, so the interpolation algorithm is necessary to achieve the data transfer of the coupling variables. The interpolation algorithm in [3] was adopted to complete the data transfer. The basic principle is mapping the grid nodes on the coupling surface from the 3D physical space to the 2D control plane, and the data transfer is achieved on the control plane. The interpolation function of wall heat flux is given by:

$$Q(u,v) = b_1u^3 + b_2v^3 + b_3u^2v + b_4v^2u + b_5u^2 + b_6v^2 + b_7uv + b_8u + b_9v + b_{10} \quad (1)$$

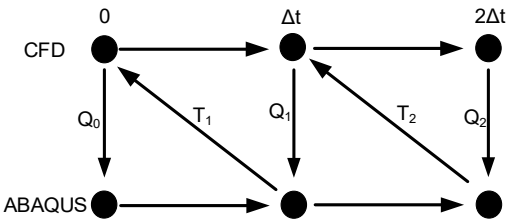

Figure 1. Transient coupled method.

2.2. Validation Example

The thermal environment of hypersonic circular tube [3] was calculated to validate the coupled method. The outer and inner diameters of the model were 76.2 mm and 50.8 mm, respectively. Table 1 presents the corresponding material properties. This paper established a 2D numerical model, and Figure 2 presents the computational grids and boundary

conditions. The red and blue zones are the flow field and structure respectively. The grid number of flow field was 300 × 200, and the grid height near the wall was 1×10^{-5} m for meeting the requirement of the Menter's SST *k*-*ω* turbulent model and obtaining wall heat flux independent of the grid height (y + <1). The parameters of hypersonic flow are shown in Table 2. In the numerical simulation, the AUSM + spatial discretization scheme with second-order accuracy [31], Menter's SST *k*-*ω* turbulent model [32] and LU-SGS time marching scheme [33] were adopted. The gas model was calorically perfect gas. Because the thermal conductivity and dynamic viscosity of the air are important for the calculation of aeroheating, the above two parameters were obtained by the corresponding Sutherland's models. The structural temperature was calculated by the ABAQUS software. The coupling analysis was transient, in which the coupled time step Δt was set to be 1×10^{-3} s and 1×10^{-4} s, and the total time of coupling analysis was 2 s. The steady flow field was taken as the initial condition for the coupling analysis, and the initial structural temperature was set as 294.4 K.

Table 1. Material properties of circular tube.

Parameter	Value	Parameter Description
k (W/(m·K))	16.72	Thermal conductivity
c (J/(kg·K))	502.48	Specific heat
ρ (kg/m^3)	8030	Density

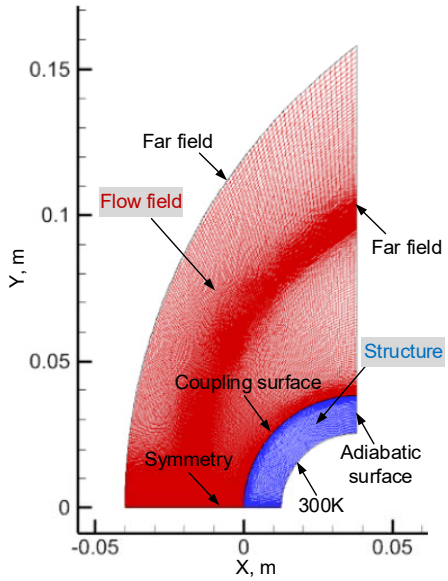

Figure 2. Computational grids and boundary conditions.

Table 2. Parameters of hypersonic flow.

Parameter	Value	Parameter Description
Ma_∞	6.47	Mach number
α (°)	0	Angle of attack
T_∞ (K)	241.5	Static temperature
p_∞ (Pa)	648.1	Static pressure

The time-history curves of the stagnation temperature under different coupled time steps were obtained (Figure 3). The stagnation temperature rose very quickly at the initial stage, and then its changing rate gradually slowed down, which will reach a stable temperature eventually (steady solution). In addition, the two time-history curves of the stagnation temperature were coincident with each other, indicating that the solution which

is independent of the coupled time step can be obtained at the coupled time step 1×10^{-3} s. Therefore, the coupled time step of 1×10^{-3} s was adopted in the subsequent analysis. The calculated dimensionless results of the outer wall are shown in Figure 4. The calculated results are in good agreement with the experimental results. Table 3 lists the calculated and experimental results of the stagnation point; the relative errors of the stagnation heat flux and stagnation temperature were 1.34% and 4.95% respectively. The above comparisons validate the accuracy of the loosely coupled method.

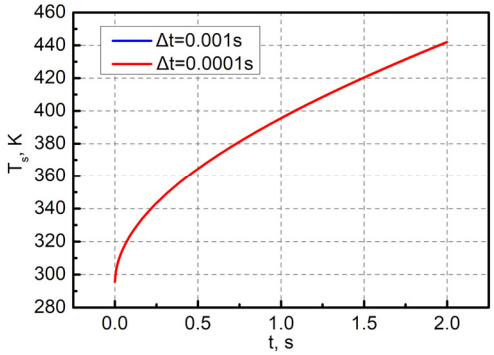

Figure 3. Variation of stagnation temperature with time.

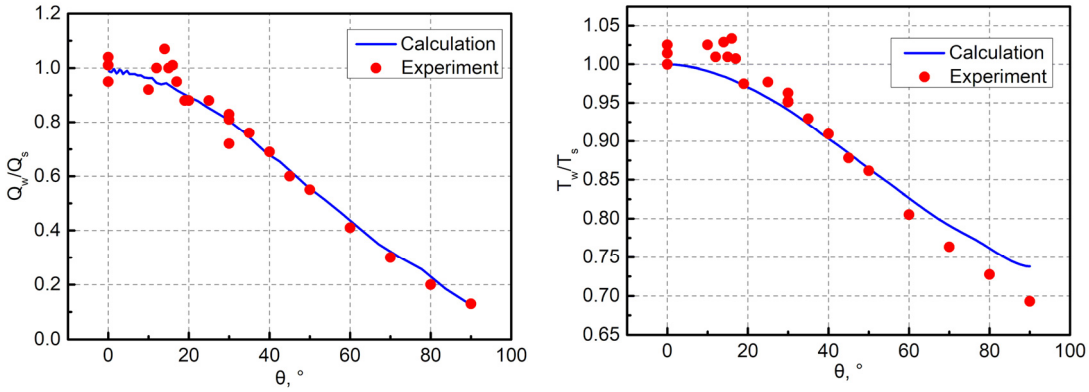

(**a**) (**b**)

Figure 4. Dimensionless heat flux and dimensionless temperature distributions of the outer wall at 2 s: (**a**) heat flux; (**b**) temperature.

Table 3. Comparison of calculated and experimental results.

Results	Quantity	Calculation	Experiment
Q_s (kW/m^2)	Stagnation heat flux	661	670
T_s (K)	Stagnation temperature	442	465

3. Geometric and Numerical Models

Figure 5 presents the geometric model in this paper, which includes a forebody, a spike, and an aerodisk. In order to study the effect of the aerodisk, a separate forebody (Model 1), a model without an aerodisk (Model 2), and two models with an aerodisk (Models 3 and 4) were constructed. Figure 6 presents the shapes and dimensions of the above models, among which Model 3 has a spherical aerodisk and Model 4 has a planar aerodisk.

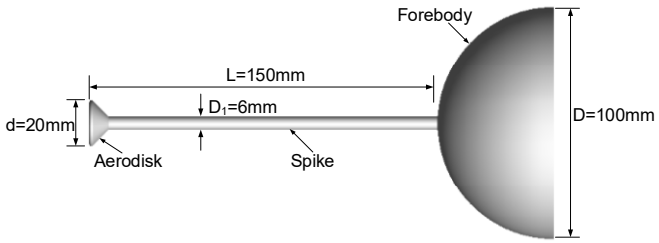

Figure 5. Typical spiked blunt body with an aerodisk.

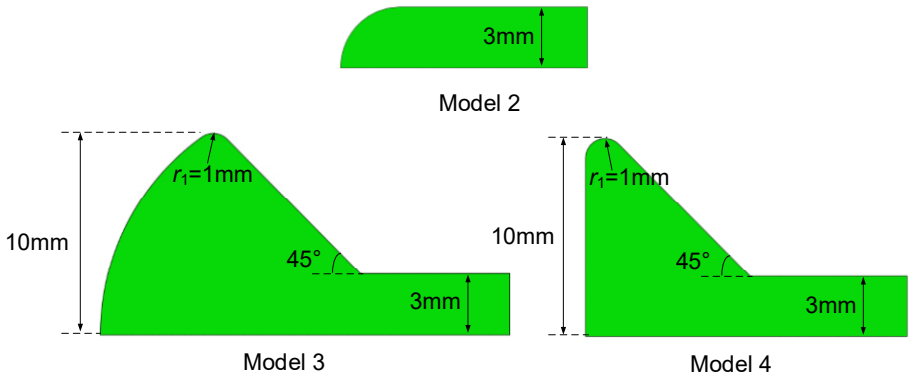

Figure 6. Different spikes.

The parameters of hypersonic flow and wall temperature T_w are shown in Table 4. This paper established the axisymmetric numerical model. Figure 7 presents the computational grids and boundary conditions, and the grid height near wall was 1×10^{-5} m in the fluid grid for obtaining wall heat flux independent of the grid height. The AUSM+ spatial discretization scheme with second-order accuracy, Menter's SST k-ω turbulent model, and the LU-SGS time marching scheme were adopted. The gas model was calorically perfect gas. The thermal conductivity and dynamic viscosity of the air were obtained by Sutherland's models. The thickness of the forebody was 15 mm, and the temperature of inner wall remained constant (300 K). Table 5 lists the corresponding material properties. The structural temperature was calculated by the ABAQUS software.

Table 4. Parameters of hypersonic flow and wall temperature.

Parameter	Value	Parameter Description
Ma_∞	8	Mach number
α (°)	0	Angle of attack
T_∞ (K)	247.02	Static temperature
p_∞ (Pa)	21.96	Static pressure
T_w (K)	300	Wall temperature

Table 5. Material thermal properties of the structure.

Parameter	Value	Parameter Description
k (W/(m·K))	2	Thermal conductivity
c (J/(kg·K))	1000	Specific heat
ρ (kg/m^3)	1500	Density

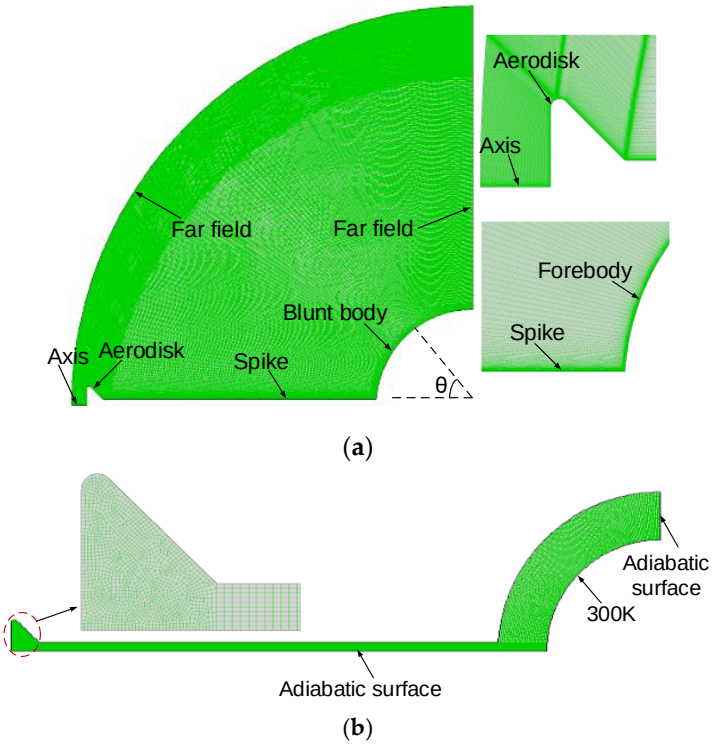

Figure 7. Computational grids of model 4: (**a**) fluid; (**b**) structure.

The grid independence study was conducted in this paper, and three grid systems were established. Figure 8 presents the wall pressure and wall heat flux of the forebody in Model 4. The results showed the calculated results had little difference between the grids 2 and 3, and the grid independent results were obtained. Therefore, grid 3 was adopted in the subsequent sections.

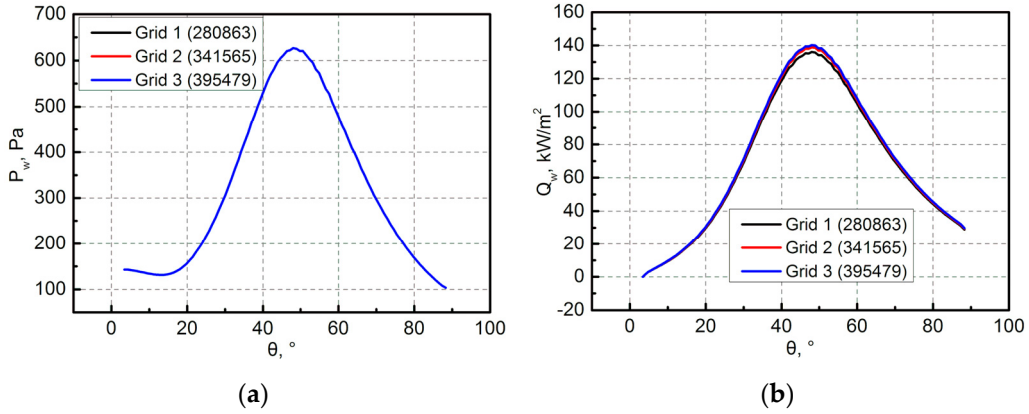

Figure 8. Grid independency analysis results: (**a**) pressure; (**b**) heat flux.

4. Results and Discussion

4.1. Comparison of Initial Results

Figure 9 presents the flow fields of different analysis models. Models 3 and 4 had the same flow characteristics as Model 2. However, influenced by the aerodisk, Models 3 and 4 had stronger bow shock waves than Model 2. In addition, Models 3 and 4 had significantly weaker reattached shock waves than Models 1 and 2, which is favorable for weakening the aeroheating of forebody. Therefore, the forebody in Models 3 and 4 had a lower peak heat flux. Although the reattached shock wave was weakened by the aerodisk, the bow shock wave in Models 3 and 4 was enhanced.

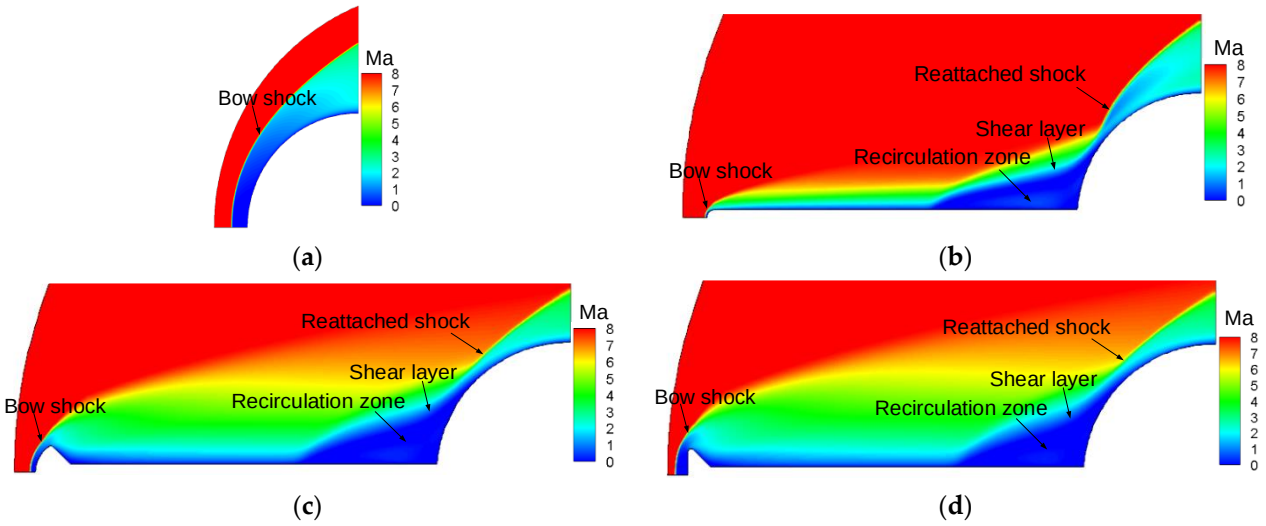

Figure 9. Flow field: (**a**) Model 1; (**b**) Model 2; (**c**) Model 3; (**d**) Model 4.

Figure 10 presents the corresponding pressure and heat flux of forebody. It was found that the peak pressure was reduced in all the three spiked models. Table 6 shows the drag coefficient of the whole model (C_d) and the peak heat flux of forebody (Q_{max}). The drag coefficients of Models 2, 3, and 4 were 5.70%, 42.26% and 48.59%, respectively, which are lower than that in Model 1. The peak heat fluxes of Models 3 and 4 were 37.80% and 46.79%, respectively, which are lower than that of Model 1, while the peak heat flux of Model 2 was 25.73% higher than that of Model 1. Therefore, the drag was reduced in Models 2, 3, and 4, and Models 3 and 4 had better drag reduction performance than Model 2. Models 3 and 4 significantly reduced the aeroheating of forebody, while Model 2 enhanced the aeroheating, which is detrimental to the thermal protection. The function of the aerodisk is enhancing the compression to hypersonic flow.

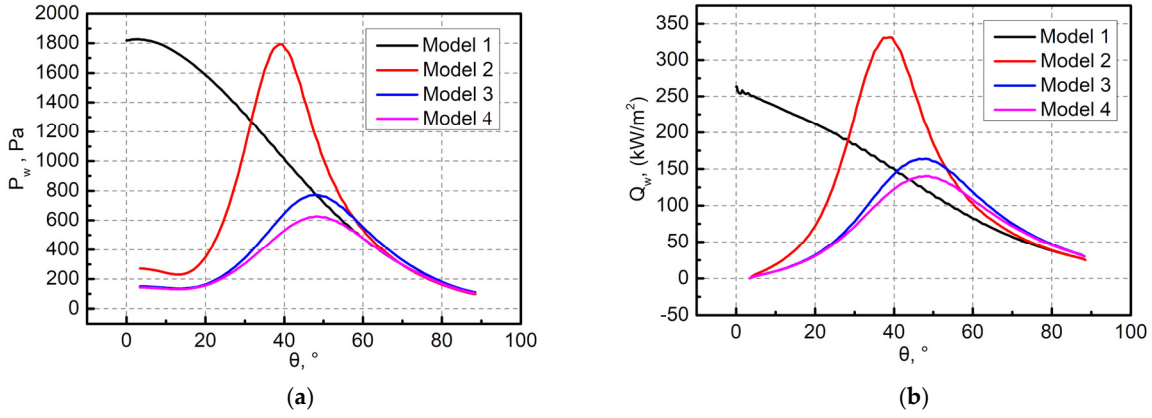

Figure 10. Initial pressure and heat flux of forebody: (**a**) pressure; (**b**) heat flux.

Table 6. Drag coefficient and peak heat flux of forebody.

Model	C_d	Q_{max} (kW/m^2)
1	0.966172	263.56
2	0.911118	331.37
3	0.557827	163.94
4	0.496696	140.25

The drag coefficients of the spike and forebody are listed in Table 7. From Model 2 to Model 4, the drag coefficient of forebody decreased gradually for the reason that the

equivalent radius of the spike increased gradually from Model 2 to Model 4, resulting in the drag coefficient of the spike increasing gradually. Since the decrease of forebody drag was much greater than the increase of spike drag, the total drag decreased gradually from Model 2 to Model 4. Table 8 presents the drag coefficient due to the viscosity and pressure. The results showed that more than 87% of the drag was caused by pressure, and only a small part was caused by the viscosity effect. In conclusion, the wall pressure distribution determines the drag coefficient.

Table 7. Influence of the spike and forebody on drag coefficient.

Model	Forebody	Spike
1	0.966172	0
2	0.901042	0.010076
3	0.502472	0.055355
4	0.427148	0.069549

Table 8. Influence of viscosity and pressure on drag coefficient.

Model	Pressure	Viscosity
1	0.900701	0.065471
2	0.820853	0.090265
3	0.486492	0.071335
4	0.434233	0.062463

4.2. Evolution of Analysis Results

The transient coupled investigations on different models were carried out, in which the coupled time step Δt was set as 1×10^{-3} s based on the conclusion drawn in Section 2.2, and the total analysis time was 20 s. The steady flow field was taken as the initial condition for coupling analysis, and the initial temperature of the structure was 300 K. The calculated results at different times are shown in Figures 11 and 12. When the coupling analysis began, the aeroheating caused the wall temperature to increase gradually, resulting in the decrease of the aeroheating according to Fourier's law. The coupled method considers the influence of wall temperature on aeroheating. The wall heat flux is always maintained at the initial value in traditional uncoupling analysis, which will cause the structural temperature to be higher than actual value. In addition, with the progress of calculation, the changing rates of the above-calculated results gradually decreased. The stationary solution will be reached when the computational time approaches infinity.

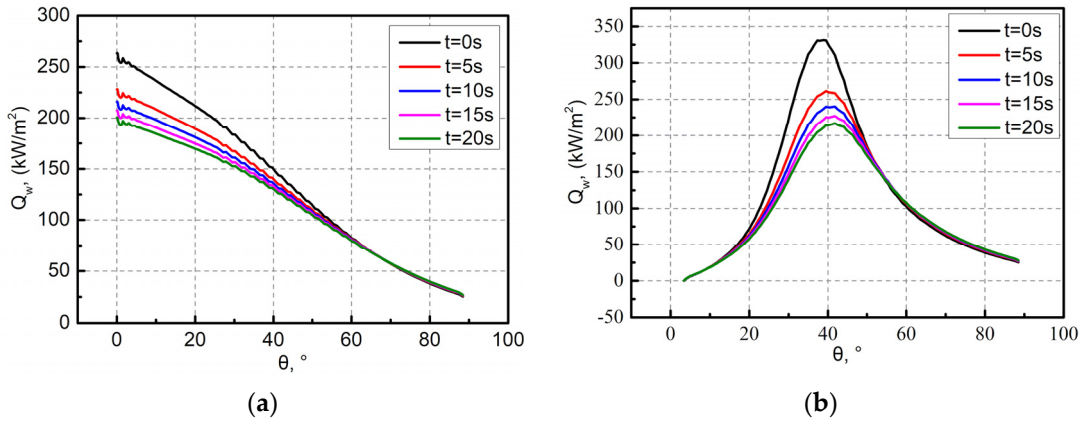

Figure 11. *Cont.*

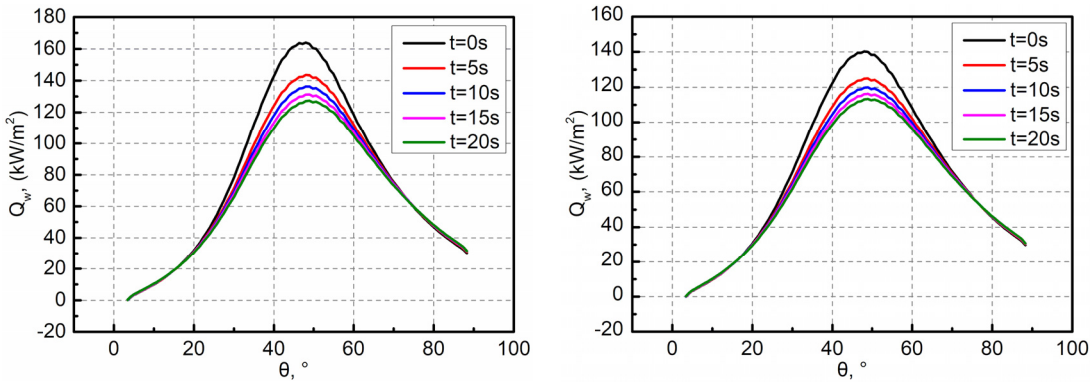

Figure 11. Evolution of wall heat flux of the forebody: (**a**) Model 1; (**b**) Model 2; (**c**) Model 3; (**d**) Model 4.

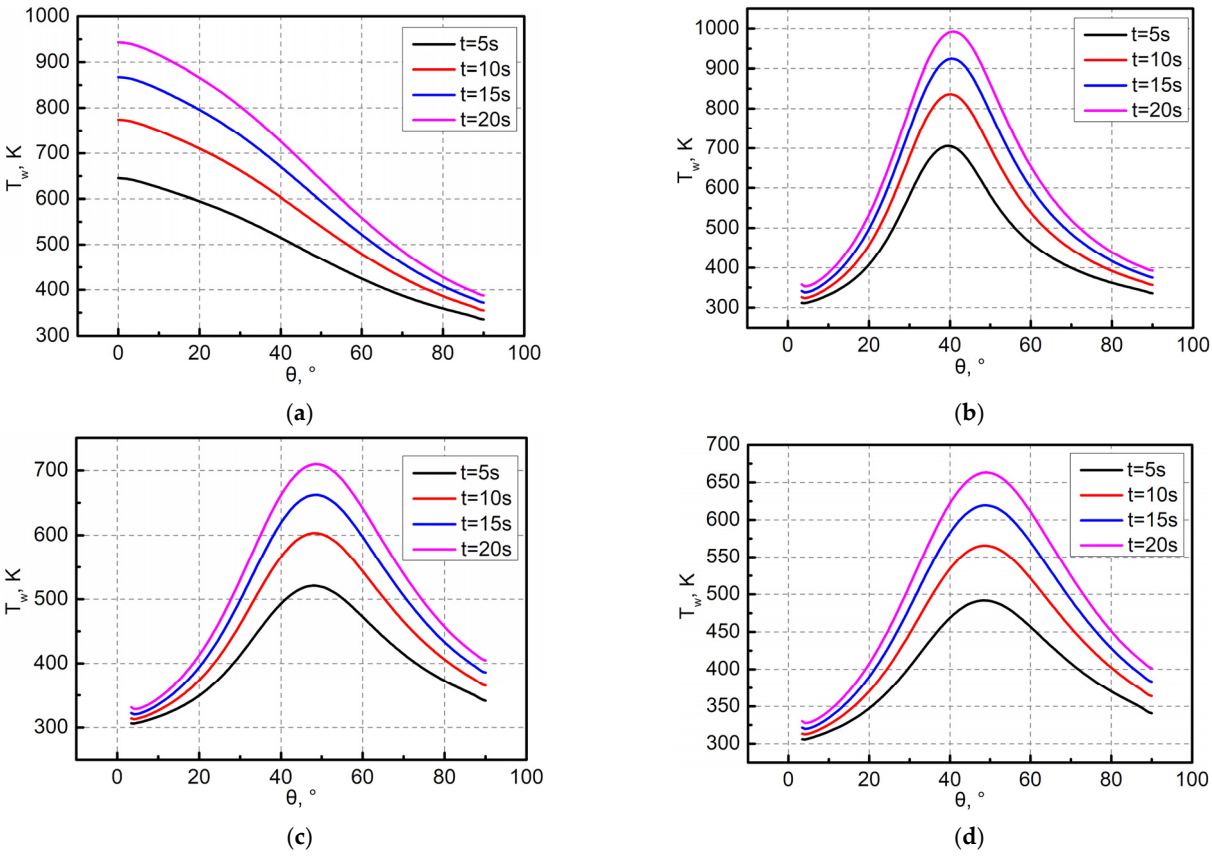

Figure 12. Evolution of wall temperature of the forebody: (**a**) Model 1; (**b**) Model 2; (**c**) Model 3; (**d**) Model 4.

Figures 13 and 14 present the temperature fields of the forebody and spike at 20 s, respectively. The maximum temperature and its position are also marked in the figures. The maximum temperature of the forebody in Model 2 was 5.24% higher than that in Model 1, and the maximum temperature of the forebody in Models 3 and 4 were 24.75% and 29.68% lower than that in Model 1, respectively. Influenced by the recirculation zone and reattached shock wave, the maximum temperature in Model 4 was the closest to the downstream, at the position of 49.11°. In addition, the maximum temperature of the spike in Model 2 reached 2366 K, while that in Models 3 and 4 were only 1600 K and 1543 K, respectively. Therefore, the spike in Model 4 had the lowest temperature and the best

non-ablative property. The maximum temperature of the spike in Models 2 and 3 was located at the stagnation point, while that in Model 4 was located at the outer edge of the aerodisk, where the curvature was at the maximum. Table 9 presents the drag coefficients of the four models at different times. It can be found that the variation of the drag coefficients of all models was less than 5% during 0~20 s. Therefore, with the progress of calculation, the change of the drag coefficient is very small, and the following sections only discuss the initial drag coefficient. The above analysis results showed that Model 4 had the best performance on the thermal protection efficiency and drag reduction efficiency.

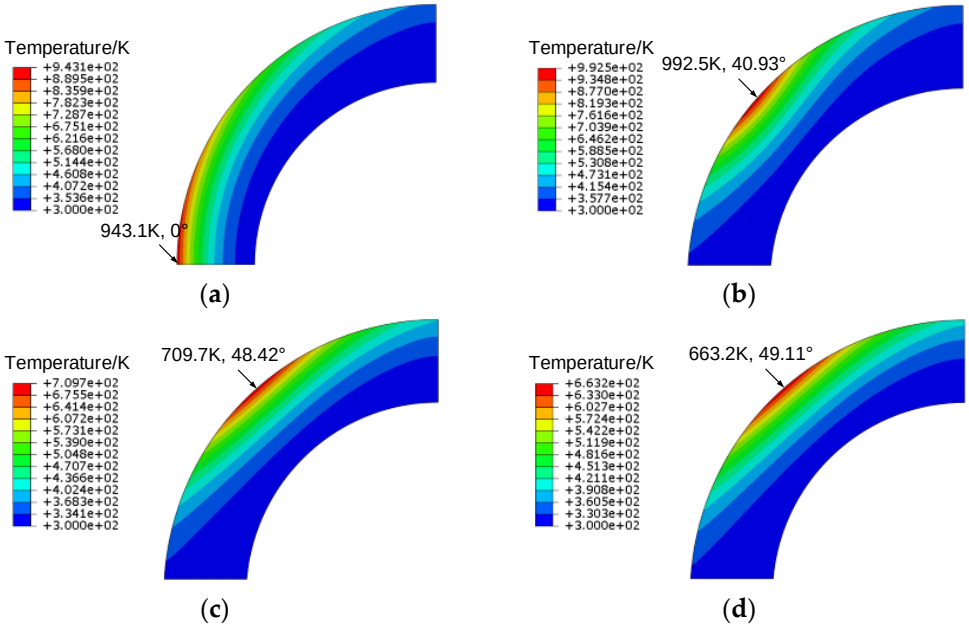

Figure 13. Comparison of structural temperature field of the forebody at 20 s: (**a**) Model 1; (**b**) Model 2; (**c**) Model 3; (**d**) Model 4.

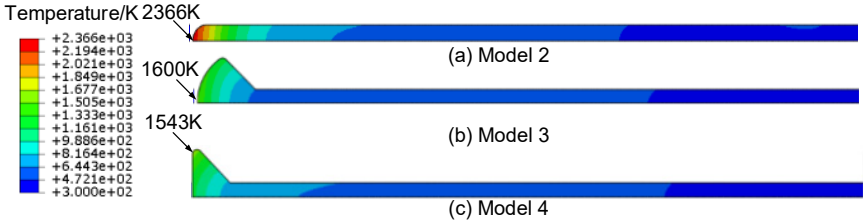

Figure 14. Comparison of the structural temperature field of the spike at 20 s.

Table 9. Evolution of the drag coefficient.

Model	1	2	3	4
t = 0 s	0.966172	0.911118	0.557827	0.496696
t = 5 s	0.968403	0.889627	0.544266	0.487179
t = 10 s	0.969502	0.879822	0.538436	0.483491
t = 15 s	0.970382	0.872595	0.533643	0.480497
t = 20 s	0.971165	0.866611	0.529479	0.477855

4.3. Effects of the Spike and Aerodisk

In Figure 5, the most important parameters are length L and diameter d. Figure 15 presents the flow fields with different length-diameter ratios L/D (D = 100 mm). When L/D was small, the influence area of the recirculation zone covered the whole flow field between the aerodisk and the forebody. As L/D increased, the recirculation zone was limited to

the flow field in front of the forebody, and the influence on the aerodisk was small with a weaker reattached shock wave.

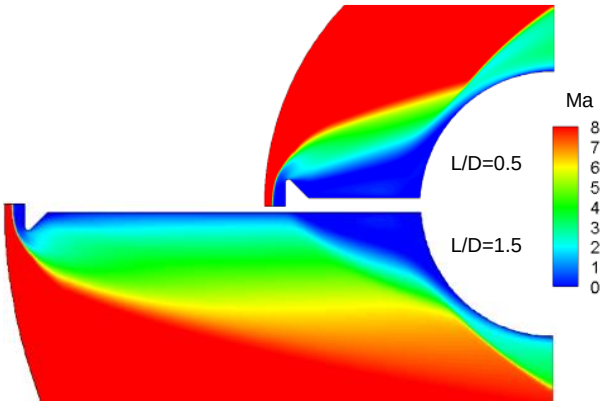

Figure 15. Effect of the length of the spike on flow field.

Figure 16 presents the corresponding initial pressure and heat flux of the forebody, indicating that the pressure and heat flux decreased with the increase of L/D. Table 10 shows the corresponding initial total drag coefficient and peak heat flux of forebody. As L/D increased from 0.5 to 2, the total drag coefficient and peak heat flux of the forebody decreased by 38.56% and 36.34% respectively, thus improving the drag and heat reduction efficiency. Figure 17 presents the corresponding temperature fields of the forebody at 20 s. As L/D increased from 0.5 to 2, the maximum temperature decreased by 20.09%, and L/D had little influence on the position of the peak temperature. In addition, the decrease rates of drag coefficient, pressure, heat flux, and temperature decreased gradually.

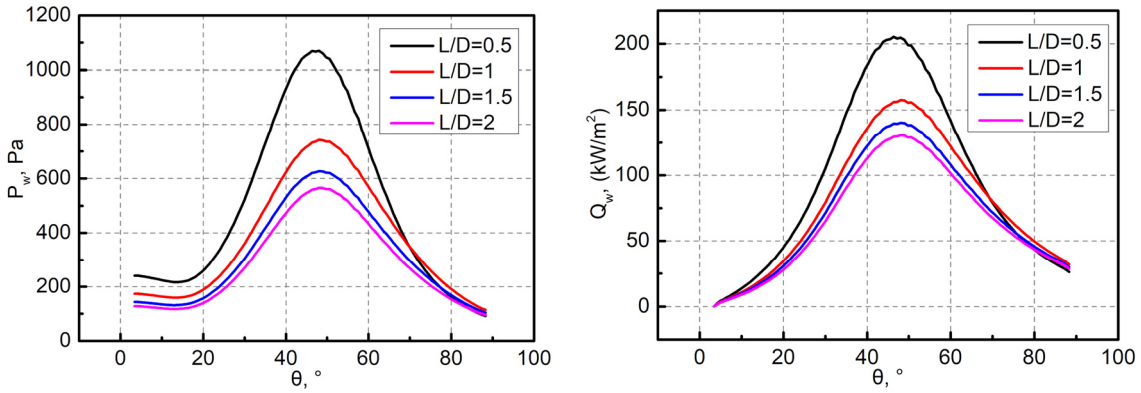

Figure 16. Initial pressure and heat flux of the forebodies with different lengths L: (**a**) pressure; (**b**) heat flux.

Table 10. Comparison of the initial total drag coefficient and peak heat flux of the forebody.

L/D	C_d	Q_{max} (kW/m^2)
0.5	0.741191	205.21
1	0.572515	157.36
1.5	0.496696	140.25
2	0.455366	130.63

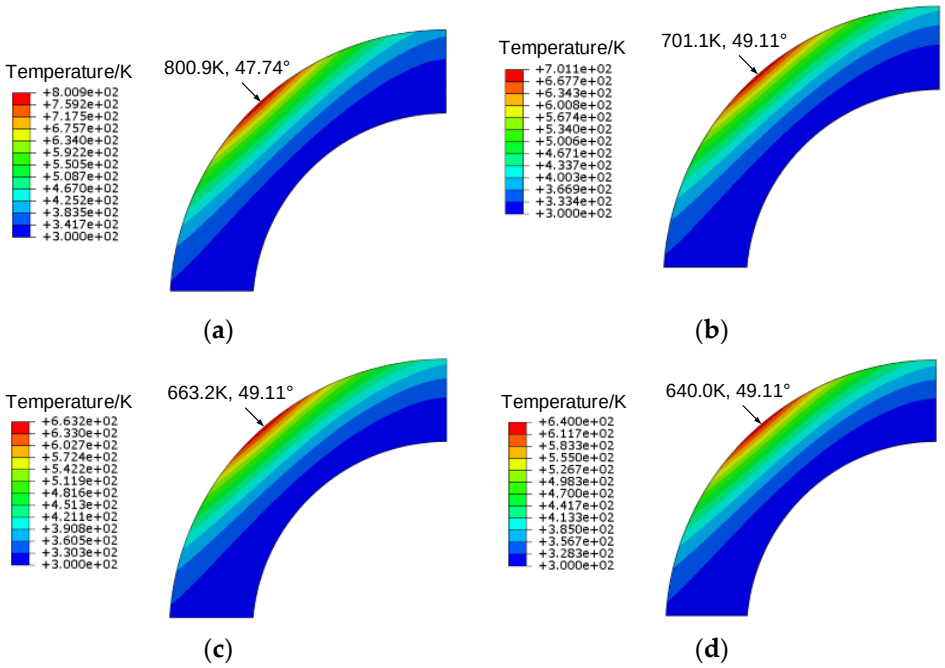

Figure 17. Comparison of the structural temperature field of the forebody at 20 s: (**a**) L/D = 0.5; (**b**) L/D = 1; (**c**) L/D = 1.5; (**d**) L/D = 2.

Figure 18 presents the flow fields with different diameters d. With the increase of d, the bow shock wave became stronger, while the reattached shock wave became weaker. In addition, the diameter d had little effect on the recirculation zone. Figure 19 presents the corresponding initial pressure and heat flux of the forebody, indicating that the pressure and heat flux will decreased with the increase of diameter d, while the decrease rates decreased gradually. Table 11 shows the corresponding initial total drag coefficient and peak heat flux of the forebody. As the diameter d increased from 24 mm to 36 mm, the peak heat flux of forebody decreased by 30.08%, thus improving the heat reduction efficiency. The total drag coefficient first decreased and then increased, which can be explained by the results in Table 12. Table 12 shows the drag coefficient of the spike and hypersonic forebody under different diameters of the aerodisks. When the diameter d was greater than a certain size, the increase of spike drag will be greater than decrease of forebody drag, and the total drag will increase gradually. Figure 20 presents the corresponding temperature fields of the forebody at 20 s. As the diameter d increased from 24 mm to 36 mm, the maximum temperature of the forebody decreased by 13.12%, and the diameter d had little influence on the position of the peak temperature.

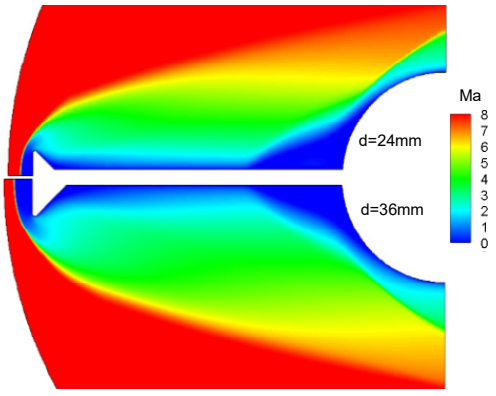

Figure 18. Effect of the diameter of the aerodisk on flow field.

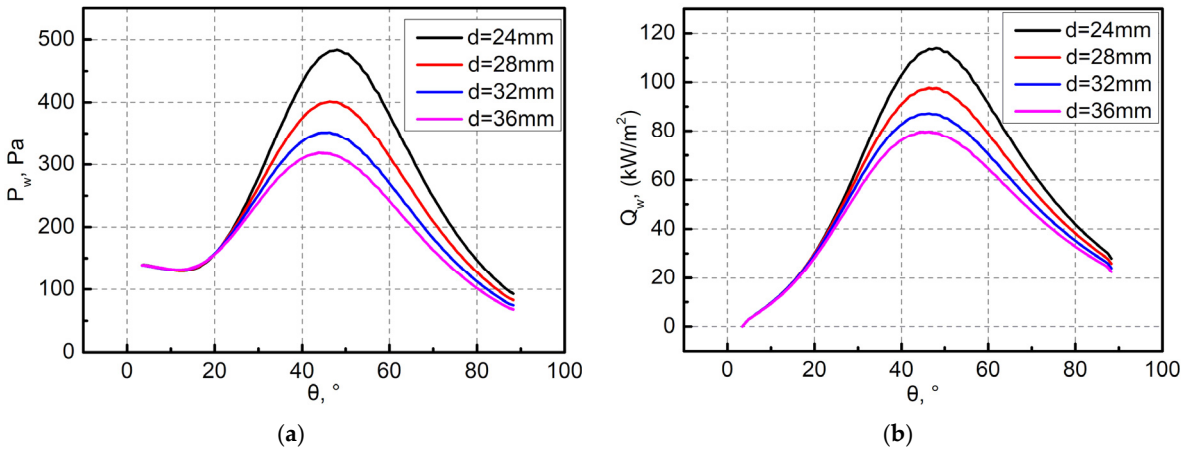

Figure 19. Initial pressure and heat flux of forebodies with different diameters *d*: (**a**) pressure; (**b**) heat flux.

Table 11. Comparison of initial total drag coefficient and peak heat flux of the forebody.

d (mm)	C_d	Q_{max} (kW/m^2)
24	0.448826	113.95
28	0.434467	97.71
32	0.442206	87.26
36	0.464701	79.67

Table 12. Drag coefficients of the spike and forebody.

d (mm)	Spike	Forebody
24	0.098819	0.350007
28	0.133358	0.301109
32	0.173247	0.268960
36	0.218722	0.245978

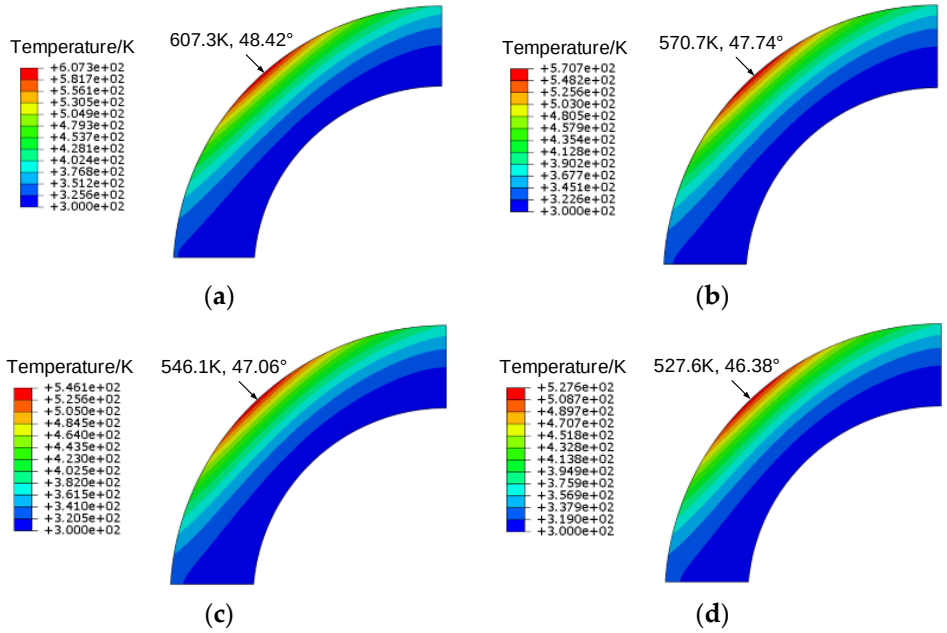

Figure 20. Comparison of the structural temperature field of the forebody at 20 s: (**a**) *d* = 24 mm; (**b**) *d* = 28 mm; (**c**) *d* = 32 mm; (**d**) *d* = 36 mm.

5. Conclusions

(1) The coupling analysis of the hypersonic circular tube was carried out. The relative errors of the stagnation heat flux and stagnation temperature between calculated and experimental results were 1.34% and 4.95%, respectively, thus verifying the calculation effectiveness of the proposed loosely coupled method in this paper.

(2) The coupling analysis had little influence on the drag coefficient. In all spiked models, more than 87% of the drag was caused by pressure, and only a small part was caused by the viscosity effect. With the progress of calculation, the changing rates of the coupled calculated results gradually decreased. The spiked model with the planar aerodisk had the least drag and the lowest temperature of the forebody; besides, the planar aerodisk also had the lowest temperature and the best non-ablative property. Influenced by the recirculation zone and reattached shock wave, the maximum temperature of the forebody in Model 4 was the closest to the downstream, at the position of 49.11°.

(3) With the increase of the length of the spike, the decrease rates of drag, pressure, heat flux, and temperature decreased gradually. Increasing the diameter of the aerodisk also reduced the temperature of the forebody, while the drag reduction efficiency increased at first and then decreased. Therefore, the heat and drag reduction must be considered comprehensively for the optimal design of the spike.

Author Contributions: Methodology, J.H.; calculation, B.F.; writing—original draft preparation, B.F.; writing—review and editing, B.F.; All authors have read and agreed to the published version of the manuscript.

Funding: This research received no external funding.

Institutional Review Board Statement: Not applicable.

Informed Consent Statement: Not applicable.

Data Availability Statement: Not applicable.

Acknowledgments: This research was supported by the Nanjing University of Aeronautics and Astronautics.

Conflicts of Interest: There are no conflict of interest in relation to this manuscript.

References

1. Hollis, B.R.; Prabhu, D.K.; Maclean, M.; Dufrene, A. Blunt-Body Aerothermodynamic Database from High-Enthalpy Carbon-Dioxide Testing in an Expansion Tunnel. *J. Thermophys. Heat Transf.* **2017**, *31*, 712–731. [CrossRef]
2. Shoev, G.; Oblapenko, G.; Kunova, O.; Mekhonoshina, M.; Kustova, E. Validation of Vibration-Dissociation Coupling Models in Hypersonic Non-Equilibrium Separated Flows. *Acta Astronaut.* **2018**, *144*, 147–159. [CrossRef]
3. Huang, J.; Li, P.; Yao, W. Thermal Protection System Gap Analysis Using a Loosely Coupled Fluid-Structural Thermal Numerical Method. *Acta Astronaut.* **2018**, *146*, 368–377. [CrossRef]
4. Oscar, A.M.; Anurag, S.; Bhavani, V.S.; Raphael, T.H.; Max, L.B. Thermal Force and Moment Determination of an Integrated Thermal Protection System. *AIAA J.* **2010**, *48*, 119–128.
5. Huang, J.; Yao, W.; Li, P. Uncertainty Dynamic Theoretical Analysis on Ceramic Thermal Protection System Using Perturbation Method. *Acta Astronaut.* **2018**, *148*, 41–47. [CrossRef]
6. Crawford, D.H. *Investigation of the Flow over Spiked-Nose Hemisphere-Cylinder at Mach Number of 6.8*; National Aeronautics and Space Administration: Washington, DC, USA, 1959; Volume 6, pp. 112–118.
7. Mair, W.A. LXVIII. Experiments on Separation of Boundary Layers on Probes in Front of Blunt-Nosed Bodies in a Supersonic Air Stream. *Lond. Edinb. Dublin Philos. Mag. J. Sci.* **1952**, *43*, 695–716. [CrossRef]
8. Maull, D.J. Hypersonic Flow over Axially Symmetric Spiked Bodies. *J. Fluid Mech.* **1960**, *8*, 584–592. [CrossRef]
9. Wood, C.J. Hypersonic Flow over Spiked Cones. *J. Fluid Mech.* **1962**, *12*, 614–624. [CrossRef]
10. Dem'yanov, Y.A.; Shmanenkov, V.N. On Studying Reverse Flows in the Zone of Separation of Turbulent Boundary Layer. *J. Appl. Math. Mech.* **1960**, *24*, 237–239.
11. Qin, Q.; Xu, J.; Guo, S. Fluid-Thermal Analysis of Aerodynamic Heating over Spiked Blunt Body Configurations. *Acta Astronaut.* **2017**, *132*, 230–242. [CrossRef]

12. Huang, W.; Li, L.Q.; Yan, L.; Zhang, T.T. Drag and Heat Flux Reduction Mechanism of Blunted Cone with Aerodisks. *Acta Astronaut.* **2017**, *138*, 168–175. [CrossRef]
13. Huang, J.; Yao, W.; Qin, N. Heat Reduction Mechanism of Hypersonic Spiked Blunt Body with Installation Angle at Large Angle of Attack. *Acta Astronaut.* **2019**, *164*, 268–276. [CrossRef]
14. Huang, W.; Chen, Z.; Yan, L.; Yan, B.B.; Du, Z.B. Drag and Heat Flux Reduction Mechanism Induced by the Spike and Its Combinations in Supersonic Flows: A review. *Prog. Aerosp. Sci.* **2019**, *105*, 31–39. [CrossRef]
15. Sun, X.; Huang, W.; Ou, M.; Zhang, R.R.; Li, S.B. A Survey on Numerical Simulations of Drag and Heat Reduction Mechanism in Supersonic/Hypersonic Flows. *Chin. J. Aeronaut.* **2019**, *32*, 771–784. [CrossRef]
16. Wang, Z.G.; Sun, X.; Huang, W.; Li, S.B.; Yan, L. Experimental Investigation on Drag and Heat Flux Reduction in Supersonic/Hypersonic Flows: A Survey. *Acta Astronaut.* **2016**, *129*, 95–110. [CrossRef]
17. Finley, P.J. The Flow of a Jet From a Body Opposing a Supersonic Free Stream. *J. Fluid Mech.* **1966**, *26*, 337–368. [CrossRef]
18. Romeo, D.J.; Sterrett, J.R. *Exploratory Investigation of the Effect of a Forward-Facing Jet on the Bow Shock of a Blunt Body in a Mach Number 6 Free Stream*; National Aeronautics and Space Administration: Washington, DC, USA, 1963; NASA TN D-1605.
19. Bushnell, D.M.; Huffman, J.K. Forward Penetration of Liquid Water and Liquid Nitrogen from the Orifice at the Stagnation Point of a Hemispherically Blunted Body in Hypersonic Flow. In *NASA TM X-1493*; NASA: Washington, DC, USA, 1968.
20. Hayashi, K.; Aso, S.; Tani, Y. Experimental Study on Thermal Protection System by Opposing Jet in Supersonic Flow. *J. Spacecr. Rocket.* **2006**, *43*, 233–235. [CrossRef]
21. Huang, W.; Jiang, Y.P.; Yan, L.; Liu, J. Heat Flux Reduction Mechanism Induced by a Combinational Opposing Jet and Cavity Concept in Supersonic Flows. *Acta Astronaut.* **2016**, *121*, 164–171. [CrossRef]
22. Huang, W.; Zhang, R.R.; Yan, L.; Ou, M.; Moradi, R. Numerical Experiment on the Flow Field Properties of a Blunted Body with a Counterflowing Jet in Supersonic Flows. *Acta Astronaut.* **2018**, *147*, 231–240. [CrossRef]
23. Huang, J.; Yao, W.; Jiang, Z. Penetration Mode Effect on Thermal Protection System by Opposing Jet. *Acta Astronaut.* **2019**, *160*, 206–215. [CrossRef]
24. Huang, J.; Yao, W.; Shan, X. Coupled Fluid-Thermal Investigation on Non-Ablative Thermal Protection System with Spiked Body and Opposing Jet Combined Configuration. *Chin. J. Aeronaut.* **2019**, *32*, 1390–1402. [CrossRef]
25. Ou, M.; Yan, L.; Huang, W.; Li, S.; Li, L. Detailed Parametric Investigations on Drag and Heat Flux Reduction Induced by a Combinational Spike and Opposing Jet Concept in Hypersonic Flows. *Int. J. Heat Mass Transf.* **2018**, *126*, 10–31. [CrossRef]
26. Huang, J.; Yao, W. A Novel Non-Ablative Thermal Protection System with Combined Spike and Opposing Jet Concept. *Acta Astronaut.* **2019**, *159*, 41–48. [CrossRef]
27. Huang, W. A Survey of Drag and Heat Reduction in Supersonic Flows by a Counterflowing Jet and Its Combinations. *J. Zhejiang Univ.-Sci. A* **2015**, *16*, 551–561. [CrossRef]
28. Huang, J.; Yao, W.; Shan, X. Numerical Investigation on Drag and Heat Reduction Mechanism of Combined Spike and Rear Opposing Jet Configuration. *Acta Astronaut.* **2019**, *155*, 179–190. [CrossRef]
29. Gerdroodbary, M.B. Numerical Analysis on Cooling Performance of Counterflowing Jet over Aerodisked Blunt Body. *Shock. Waves* **2014**, *24*, 537–543. [CrossRef]
30. Huang, J.; Yao, W. Active Flow Control by a Novel Combinational Active Thermal Protection for Hypersonic Vehicles. *Acta Astronauti.* **2020**, *170*, 320–330. [CrossRef]
31. Liou, M.S. A sequel to AUSM: AUSM+. *J. Comput. Phys.* **1996**, *129*, 364–382. [CrossRef]
32. Menter, F.R. Two-Equation Eddy-Viscosity Turbulence Models for Engineering Applications. *AIAA J.* **1994**, *32*, 1598–1605. [CrossRef]
33. Yoon, S.; Jameson, A. Low-upper symmetric-Gauss-Sediel method for the Euler and Navier-Stokes equations. *AIAA J.* **1998**, *26*, 1025–1026. [CrossRef]